Journal of Natural Gas Science and Engineering 80 (2020) 103378

Contents lists available at ScienceDirect

Journal of Natural Gas Science and Engineering

journal homepage: http://www.elsevier.com/locate/jngse

Population-balance modeling of CO_2 foam for CCUS using nanoparticles

Øyvind Eide [a], Martin Fernø [a], Steven Bryant [b], Anthony Kovscek [c], Jarand Gauteplass [a,*]

[a] Department of Physics and Technology, University of Bergen, Norway
[b] Department of Chemical and Petroleum Engineering, University of Calgary, Canada
[c] Department of Energy Resources Engineering, Stanford University, USA

ARTICLE INFO

Keywords:
CCUS
CO_2 foam
Nanoparticles
Population-balance modeling
Foam texture

ABSTRACT

Foam implementation for carbon capture, utilization and storage (CCUS) can greatly improve CO_2 mobility control, resulting in enhanced hydrocarbon production and carbon storage capacity. The use of nanoparticles (NP) to create robust foam structures has recently gained attention. Local foam generation and coalescence dynamics can be described by mathematical models. Here we address knowledge gaps for NP foam in porous media by tracking the bubble density (n_f) of NP foam data spatially and temporally using an established surfactant (SF) population-balance model. We suggest a reduced shear-thinning effect, compared to SF, to accurately model NP CO_2 foam flow in both the high- and low-quality regime. A NP foam rheological transition appeared at gas fraction $f_g = 0.85$. The n_f parameter increased linearly with distance from inlet for NP foam, with reduced CO_2 mobility and improved displacement efficiency compared to co-injections of water and CO_2.

1. Introduction

Carbon geo-sequestration can benefit from improved CO_2 mobility control during fluid displacements and flow in porous media. Reduced gravity override and viscous fingering due to CO_2 foam generation leads to improved volumetric sweep in hydrocarbon reservoirs and carbon storage sites. Thus, a successful implementation of CO_2 foam flow enhances carbon storage capacity and hydrocarbon production compared to conventional low-viscous gas flooding. A key success criterion for CO_2 foam displacement is developing stable and strong foam structures. Surfactants (SF) are typically used to stabilize the lamellae separating individual CO_2 bubbles, demonstrating excellent properties as a foaming agent, albeit suffering from great adsorption loss and often becoming weakened by challenging reservoir conditions. Therefore, the emerging trend of using tailored nanoparticles (NP) to create more robust foam structures has received a lot of attention recently (Binks and Lumsdon, 2000; Dickson et al., 2004; Sun et al., 2017; Yekeen et al., 2018; Rognmo et al., 2019). While NP are usually less effective at generating foam compared with SF, the mechanical and thermal stability of NP make them more tolerant against high temperatures, pressures, shear and salinity (Bennetzen and Mogensen, 2014). NP at interfaces are associated with high surface adsorption energies that practically eliminate them from being desorbed (Binks, 2002), adding stability to CO_2 foam flow in porous media. Further, co-injecting silica NP solution with CO_2 lowers the pH of the mixture, reported to reduce the overall risk of NP aggregation (Kim et al., 2015).

SF foam has been characterized extensively, and much is known about the foam behavior and rheology, particularly without the presence of oil (Bernard et al., 1980; Hirasaki and Lawson, 1985; Khatib et al., 1988). Foam is created by leave-behind, lamellae division and snap-off mechanisms, and the stability of foam in porous media is limited by capillary pressures (Khatib et al., 1988). A detailed description of foam creation and destruction mechanisms can be found elsewhere (Nguyen et al., 2000). Flowing SF foam is frequently reported to exhibit a shear-thinning behavior (Hirasaki and Lawson, 1985; Khatib et al., 1988; Marsden and Khan, 1966; Heller and Kuntamukkula, 1987; Falls et al., 2007; Fernø et al., 2016), explained by bubbles slipping on the pore wall and against each other. NP foam is less studied and the literature contain sparse information on NP flow properties, especially in porous media. Several authors report near-Newtonian NP foam behavior (Lotfollahi et al., 2016a; AlYousif et al., 2018), whereas others state a clear shear-thinning effect (Griffith et al., 2016; Worthen et al., 2015), in contrast to reported shear-thickening effects (Mo et al., 2012).

Predictive mathematical models are needed to describe foam flow in porous media accurately, currently underdeveloped for NP foam, for large-scale implementation of CO_2 foam in CCUS applications. Specifically, population-balance models have the unique potential to describe both transient and steady-state conditions for foam flow by spatially and

* Corresponding author.
E-mail address: Jarand.Gauteplass@uib.no (J. Gauteplass).

https://doi.org/10.1016/j.jngse.2020.103378
Received 6 November 2019; Received in revised form 14 May 2020; Accepted 14 May 2020
Available online 20 May 2020

temporally tracking the bubble density (n_f). The n_f parameter is a function of generation and coalescence mechanisms, and is of great significance as bubble density/texture is directly coupled to flow resistance (Ettinger and Radke, 1992). This paper expands the application of an established population-balance model by including NP CO_2 foam data to improve characterization of dynamic bubble densities containing nanoparticles in the pore network. The paper is structured to first introduce the experimental data used for core-scale history matching. Then, the population-balance model and key parameters are presented. Further, we tuned the mechanistic model by adjusting specific kinetic terms introduced in section 1.2 to match the laboratory observations. Lastly, we characterized NP foam properties and directly compared the results with a baseline (no foaming agent) and a SF foam flood.

1.1. Experimental data

The experimental CO_2 foam flow data in this paper are based on earlier work from the same research group (Rognmo et al., 2017; Horjen, 2015; Rognmo, 2018). Co-injections of liquid CO_2 and a foaming solution (NP or SF dispersed in brine) were performed in two Bentheimer sandstone core samples (Table 1) to generate either NP CO_2 foam or SF CO_2 foam for a range of gas fractions and total injection rates. The pore pressure and temperature were 90 bar and 20 °C, respectively.

The sandstone core samples were fully saturated with foaming solutions (Table 2) prior to co-injections. The SF solution consisted of $C_{14\text{-}16}$ alpha olefin sulfonate (AOS, Stepan Company) dispersed in brine. To generate NP foam in porous media, particle concentration and shear rate should exceed a threshold value to maintain foam stability (Espinoza et al., 2010). Moreover, particle hydrophobicity can affect NP foam generation rate and bubble size/texture (Yu et al., 2014), and the silane-modified silica particles used herein (Levasil CC301, provided by Nouryon) obtained a hydrophilic surface (Rognmo et al., 2017). The small mean particle diameter (Table 2) allowed NP to flow unrestricted through the Bentheimer pore network, and NP foam appeared stable (low coalescence rate) at concentrations ranging from 0.15 to 0.5 wt% particles dispersed in brine at experimental conditions (Rognmo, 2018).

The effective (apparent) gas viscosity, μ_f, was derived from experimental data by the expression:

$$\mu_f = \frac{k\Delta p}{(u_l + u_g)} \tag{1}$$

where k is permeability of the porous medium, Δp is the pressure gradient across the medium, and u_l and u_g is velocity of liquid and gas, respectively. Gas fraction (f_g) is commonly referred to as foam quality, and is the ratio of flowing gas rate (q_g) to total injection rate ($q_g + q_l$):

$$f_g = \frac{q_g}{q_g + q_l} \tag{2}$$

Co-injections with NP solution and CO_2 used three different total volumetric injection rates (120, 180 and 240 ml/h) at $f_g = 0.1$, 0.2, 0.35, 0.5, 0.7, 0.85, 0.9 and 0.99 during drainage (increasing gas fraction). Co-injections with SF solution and CO_2 foam used two different total volumetric injection rates (120 and 180 ml/h), at $f_g = 0.1$, 0.5, 0.7, 0.9, 0.95 and 1.0 during drainage. The maximum effective viscosity for NP foam quality scan, expressed as effective viscosity as function of increasing f_g, was observed at $f_g = 0.7$ (Fig. 2), compared with $f_g = 0.9$ for SF foam. Further, NP foam showed near-Newtonian flow (similar effective viscosity for all injection rates), whereas SF foam demonstrated the expected shear-thinning behavior (lower effective viscosity for higher injection rates). The effective viscosity was approximately two orders of magnitude higher compared than NP foam (Rognmo et al., 2017).

Table 1
Rock properties from (Rognmo et al., 2017) used as input in the population-balance model.

Core ID	Length [cm]	Diameter [cm]	Porosity [%]	Permeability [mD]	Foam stabilizer
ST3	28.80	3.77	23.81	2252	NP solution
ST6	27.60	3.77	22.74	1798	SF solution

Table 2
Fluid properties from (Rognmo et al., 2017) used as input in the population-balance model.

Fluid	Composition
Brine	2.0 wt% NaCl in distilled water
Gas	CO_2 (99.999% quality, 5.0 Ultra)
NP solution	0.15 wt% NP in brine Particle diameter ≈ 23 nm
SF solution	1.0 wt% AOS in brine

We propose that the reported experimental results of NP CO_2 foam flow is due to a reduced number of foam bubbles and reduced surface interaction compared with SF CO_2 foam. This is corroborated by comparing pore-scale bubble density between SF and NP CO_2 foam at similar experimental conditions using a high-pressure silicon micromodel, since reliable *in situ* bubble density in opaque core systems are very difficult to obtain. Direct comparison of foaming agents (Fig. 1) demonstrated quantitatively a substantial reduced bubble count for NP CO_2 foam (Benali, 2019) at equal PV CO_2 injected. Foam bubble density analysis (baseline = 45 bubbles, SF foam = 506 bubbles, NP foam = 366 bubbles) revealed that both surfactants and nanoparticles were able to generate strong foam compared to the baseline without foaming agent (no stable bubbles). NP CO_2 foam bubbles were spherical in shape and heterogeneously distributed, whereas SF CO_2 foam generated a higher number of pore-spanning lamellae that were uniformly distributed in the pore network. Bubble size generally defines the foam texture (n_f) which significantly affects the foam flow properties. Finer foam texture (higher n_f) implies lower gas mobility (Kovscek and Radke, 1994).

1.2. Model description

In this study we use a well-established SF population-balance model to simulate CO_2 foam flow (Chen et al., 2010; Kovscek et al., 1995). The model keeps track of the number of foam bubbles in the porous media and adjust the effective gas viscosity accordingly. In a one-dimensional porous medium, the mass balance of foam bubbles can be expressed as:

$$\frac{\delta}{\delta t}\left[\varphi\left(S_f n_f + S_t n_t\right)\right] + \frac{\delta}{\delta t}\left(u_f n_f\right) = \varphi S_g \left(k_1 \left| v_w v_f^{\frac{1}{3}} \right| - k_{-1} \left| v_f \right| n_f \right) + Q_b \tag{3}$$

where φ is porosity, S_f is flowing gas saturation, n_f is foam texture/bubbles per unit of flowing gas, S_t is trapped gas saturation, n_t is foam bubbles per unit of trapped gas, and u_f is Darcy velocity. S_g is the sum of flowing and trapped gas saturation ($S_g = S_f + S_t$), k_1 is foam generation rate, k_{-1} is foam coalescence rate, v_w is interstitial velocity of water, v_f is interstitial velocity of gas, and Q_b is a source/sink term for foam bubbles. Because no foam was pre-generated in the system, Q_b is set to 0. Expressions for standard multiphase form of Darcy's law and relative permeability formulations with standard Corey exponent models can be found in Supplementary material and in the original model (Kovscek et al., 1995).

Foam generation rate is written as:

$$k_1 = k_1^0\left[1 - \left(\frac{n_f}{n^*}\right)^{\omega}\right] \tag{4}$$

where k_1 is the foam generation rate, k_1^0 is a foam generation constant, n_f is foam texture, n^* is limiting foam texture and ω determines the function type of foam generation. Because limiting foam texture depends on

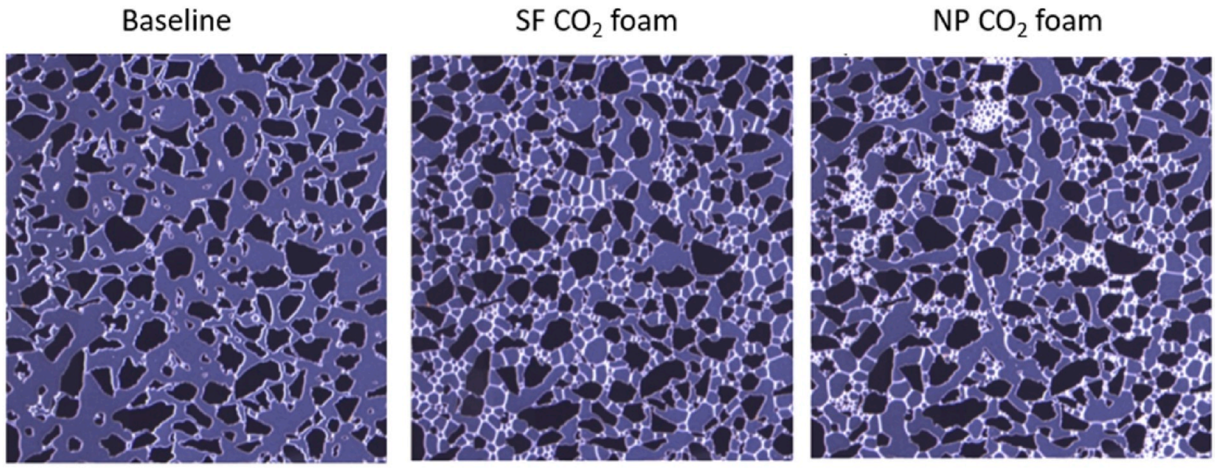

Fig. 1. The effect of different foaming agents on pore-scale bubble density (white lines = lamellae). Micromodel image series (Benali, 2019), showing a baseline (CO_2 and water – left image) in sandstone pore network (grains = black shapes) without foaming agent, SF CO_2 foam (middle) and NP CO_2 foam (right). Quantitative bubble density analysis (baseline = 45 bubbles, SF foam = 506 bubbles, NP foam = 366 bubbles) revealed that both surfactants and nanoparticles were able to generate strong foam compared to the baseline (no foaming agent) where the CO_2 phase remained continuous in the pore system.

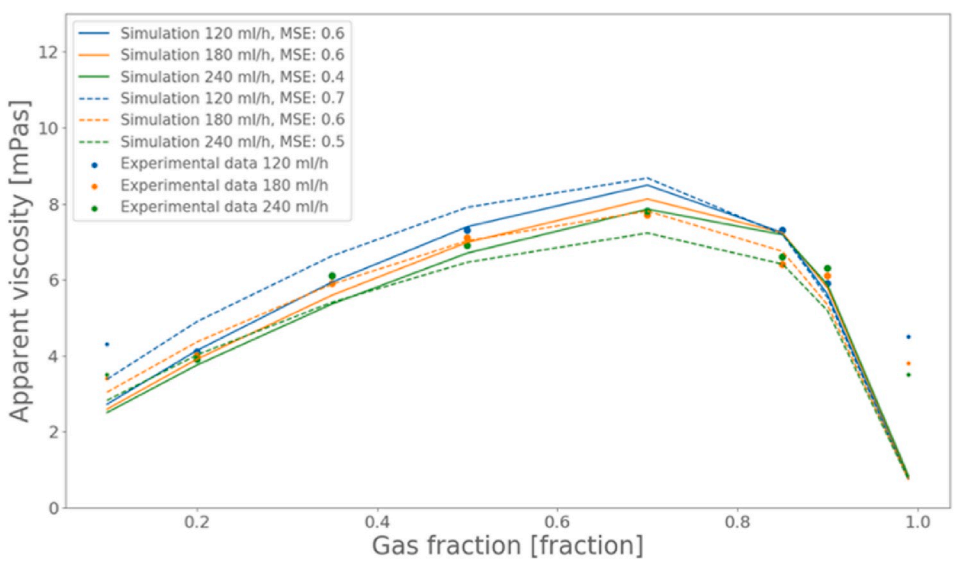

Fig. 2. Simulated (lines) and experimental (points) NP foam effective viscosities, μ_f, for three different total flow rates (120, 180, and 240 ml/h), with theoretical shear-thinning velocity exponent $c = 1/3$ (broken lines) and near-Newtonian flow behavior $c = 1/5.5$ (solid lines). Degree of match is displayed as mean squared error (MSE). Lowest (f_g=0.1) and highest gas fraction (f_g=1.0) has not been emphasized in the history matching due to experimental uncertainties. The highest effective viscosity in the foam quality scans was observed at $f_g = 0.7$, independent of total flow rate.

rock properties and we assume one bubble per pore (Ettinger and Radke, 1992; Bertin et al., 1998), n^* was kept constant at 4000 mm^{-3} for all simulations, both SF and NP CO_2 foam. Foam coalescence rate can be expressed as:

$$k_{-1} = k_{-1}^0 \left(\frac{P_c}{P_c^* - P_c} \right)^2 \quad (5)$$

where k_{-1} is foam coalescence rate, k_{-1}^0 is a scaling constant, P_c is capillary pressure and P_c^* is limiting capillary pressure for foam coalescence. The limiting capillary pressure is dependent on foaming agent concentration and can be expressed as:

$$P_c^* = P_{c,max}^* tanh\left(\frac{C_s}{C_s^0} \right) \quad (6)$$

where $P_{c,max}^*$ is a limiting value for P_c^*, C_s is the foaming agent concentration and C_s^0 is a concentration threshold for strong foam generation. When the core is pre-saturated with a foaming solution, it is assumed that the concentration is uniform and rock adsorption is satisfied. In this instance, the foaming agent mass balance is automatically satisfied (Kovscek et al., 1995). The effective (apparent) gas viscosity can be expressed as:

$$\mu_f = \mu_g + \frac{\alpha n_f}{|v_f|^c} \quad (7)$$

where μ_f is effective gas viscosity (subscript f denotes flowing foam), μ_g is gas viscosity, α is the viscosity proportionality constant, n_f is foam bubbles/texture, v_f is gas velocity and c is a velocity exponent which is theoretically close to $\frac{1}{3}$ for shear thinning foams (Hirasaki and Lawson, 1985; Kolb and Cerro, 2002). This relationship in Eq. (7) means that increasing number of foam bubbles increases effective foam viscosity, and inversely, at insignificant bubble number and high gas velocity the initial gas viscosity is recovered ($\mu_f = \mu_g$). The fraction of foam trapped, X_t, can be written as:

$$X_t = X_{t,max} \left(\frac{\beta n_t}{1 + \beta n_t} \right) \quad (8)$$

where $X_{t,max}$ is maximum fraction of trapped foam, n_t is foam bubbles per unit of trapped gas, and β is a trapping parameter. Capillary pressure was modelled using the Leverett-J function (Leverett, 1941):

$$J(S_w) = \frac{P_c}{\sigma}\sqrt{\frac{k}{\varphi}} \tag{9}$$

where P_c and σ are capillary pressure and interfacial tension respectively, between the phases CO_2 and water, k is permeability and φ is porosity. The aqueous solution is assumed to be incompressible, whereas the gas density scales linearly with pressure. Several different population-balance models exist, e.g. (Falls et al., 1988; Chang et al., 1990; Kam and Rossen, 2003), but the key characteristics are similar. The differences between various models are typically the dominant foam generation mechanism (Ma et al., 2015), and the effect of oil on foam stability (Hematpur et al., 2018). The experimental data presented in this paper did not include an oil phase. All existing foam models, population-balance versions and implicit-texture versions, provide non-unique solutions (Lotfollahi et al., 2016b), however, the parameters chosen here are derived from physical observations.

2. Simulation results and discussion

A one dimensional (1D) model with 50 cells was created to replicate the core sample reported in the laboratory co-injections using rock and fluid parameters in Tables 1 and 2. The injection strategy reflected reported experimental conditions, described as co-injection of either 1) water and CO_2 (baseline; no foaming agent), 2) NP solution and CO_2, or 3) SF solution and CO_2. Limiting foam texture was set to 4000 mm^{-3} based on pore size of 0.07 mm for pores with foam, and cubical packing of the foam bubbles. Cubical packing was used because the limiting foam texture is associated with wet foam where the shape tends to be spherical (Ettinger and Radke, 1992; Alvarez et al., 2001; Belyadi et al., 2017). The average pore size in the model was based on pore size distribution measurements in Bentheimer sandstone (Peksa et al., 2015), corroborating values reported elsewhere (Liaw et al., 1996; Barifcani et al., 2015). Overview of parameters used in the population-balance model (Kovscek et al., 1995) are presented in Table 3.

2.1. History-matching experimental data

The matching procedure for the population-balance model required an effective viscosity profile obtained at steady state (presented in Fig. 2), along with the accompanying subset data of pressure gradient vs volumetric gas rate at fixed water rate (presented in Fig. 3a), and the pressure gradient vs volumetric water rate at fixed gas rate (presented in Fig. 3b). Often, these data sets can be obtained within one experimental run (Kovscek et al., 1995). Steady-state conditions were not met for endpoint f_g in the available laboratory co-injection raw data (Horjen, 2015), see Supplementary material for transient pressure data. Here, the differential pressure was still declining when f_g was changed; hence, we expect the effective viscosity, μ_f, to be lower than reported in (Rognmo et al., 2017) at $f_g = 0.1$ and $f_g = 0.99$. The experimentally measured data points without true steady-state conditions are indicated using smaller-sized points to reflect the lower confidence for the reported effective viscosities for these f_g. NP foam effective viscosities simulated using the theoretical velocity exponent of $c = 1/3$ matched the reported experimental data set moderately, with μ_f gradually increasing with increasing gas fraction (Fig. 2 – broken lines). Maximum gas mobility reduction occurred at $f_g = 0.7$, followed by a gradual destruction of foam bubbles dictated by the capillary forces as foam quality approaches unity. The population-balance model reproduce the experimental trends with lesser degree of match at $f_g = 0.1$ and $f_g = 0.99$, however this is likely due to the aforementioned unfulfilled steady-state conditions. The experimentally measured effective viscosities (marked as data points) appear to be insensitive to total injection rate for each f_g, whereas a flow rate dependency was observed in simulated data with decreasing viscosity with increasing total flow rate at fixed foam quality for most of the gas fraction interval.

Table 3
List of foam flow and model parameters.

	Notation	Description	Values (NP vs SF)
Model parameters	c	Velocity exponent for effective gas viscosity	NP = 1/5.5 SF = 1/3
	α	Viscosity proportionality constant	NP = 1.10×10^{-16} SF = 4.05×10^{-17}
	k_1^0	Foam generation rate	3.688×10^{14} $s^{1/3}$ $m^{-13/3}$
	ω	Foam generation exponent	3
	k_{-1}^0	Foam coalescence rate	24.51 m^{-1}
	C_s	Foaming agent concentration	NP = 0.15 wt% SF = 1.0 wt%
	C_s^0	Concentration threshold	0.083 wt%
	n^*	Limiting foam texture	4000 mm^{-3}
	β	Trapping parameter	1.0×10^{-9} m^3
	$X_{t,max}$	Max fraction of trapped foam	0.90
	$P_{c,max}^*$	Max capillary pressure	3.0×10^4 Pa
	Q_b	Source/sink term	0
Flow parameters	k_{rg}^0	End point gas relative permeability	1.0
	k_{rw}^0	End point water relative permeability	0.70
	g	Corey exponent for gas	3.0
	f	Corey exponent for water	3.0
	S_{wc}	Connate water saturation	0.25
	μ_g	Gas viscosity	0.079 mPa s
	μ_w	Water viscosity	1.03 mPa s

The effective gas viscosity, μ_f, in the model is calculated using Eq. (7), where the default value gives a rate dependency and non-Newtonian behavior of the flowing foam. As stated in the introduction section, shear-thinning behavior is observed for most SF foam where the pore wall is coated with surfactants causing the bubbles to slip at high shear. Shear thinning is also observed in other emulsion systems, both in bulk and porous media, for example oil-in-water emulsions (Zhang et al., 2010; Karambeigi et al., 2015; Zhou et al., 2017). In addition to bubble slipping, shear thinning has also been attributed to bubble size dependence on flow rate (Zhou et al., 2017). At low injection rate and large bubble size, high μ_f was observed as bubbles blocked pore throats, in contrast to higher rates and reduced bubble size where the emulsions could more easily flow in the porous media. Recent literature data on flow rate dependency on NP foam is not coherent: shear-thinning properties in glass bead pack is reported (Xiao et al., 2017), but others found little evidence of shear-thinning viscosity with particle diameters above 12 nm (Kim et al., 2016). Low sensitivity of flow rates was reported for both shear-thinning and shear-thickening behavior for NP foam (AlYousif et al., 2018).

In accordance with our own experimental data and recent observations reported by others, the effect of flow rate on effective viscosity (expressed through the velocity exponent c) was reduced from the default value in the model to replicate reported NP CO_2 foam behavior. Decreasing the exponent c from 1/3 to 1/5.5 required an increase in the proportionality constant α from Eq. (7), to compensate for the overall decrease in μ_f. By keeping the exponent above zero we retain some shear dependence, as observed in experiments at similar flow rates (Horjen, 2015), and the degree of match was improved (Fig. 2 – solid lines). The proportionality constant α was increased from 4.05×10^{-17} for shear-thinning foam systems (Fig. 2 - broken lines) to 1.10×10^{-16} for near-Newtonian NP foam (Fig. 2 - solid lines). The change in viscosity and subsequent increase of α, implies that when NP CO_2 foam becomes

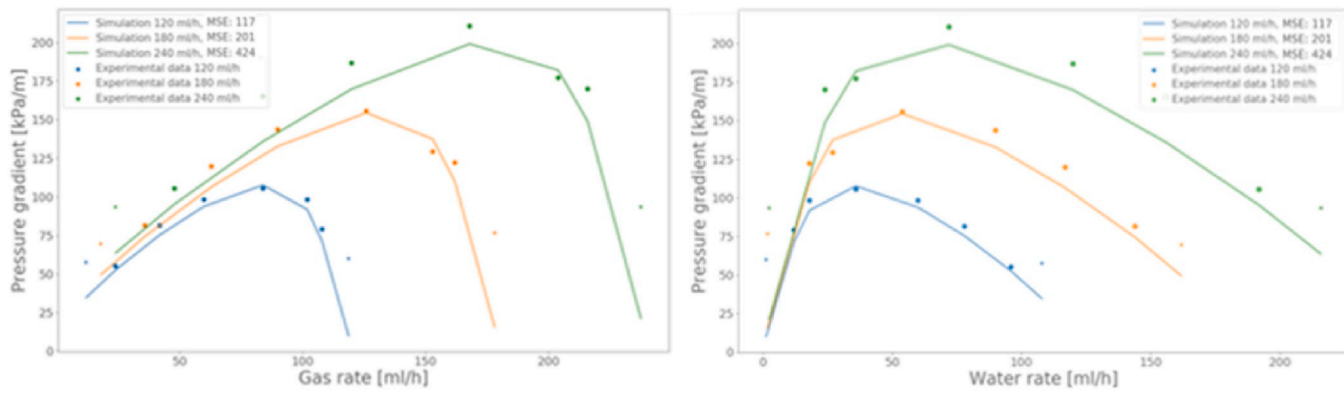

Fig. 3. Comparison of experimental (points) and simulated (lines) NP foam data, displayed as pressure gradient versus gas injection rate at fixed water rate (3a - left) and pressure gradient versus water injection rate at fixed gas rate (3b - right), MSE values correspond to 117 (120 ml/h), 201 (180 ml/h), and 424 (240 ml/h).

less shear thinning it also becomes stronger at equivalent flow rate and gas fraction. The rheology of NP CO_2 foam is further discussed in section 2.2.

The experimental data from (Horjen, 2015) has also been simulated using a different population-balance approach, focusing on the gas fraction interval $f_g = 0.5$ to 1.0 (Ortiz et al., 2019). The authors achieved good agreement between experimental and simulated data, however the model relied on limiting water saturation to separate the high and low-quality regime, using different velocity exponents to separate the degree of non-Newtonian viscosity in the two regimes. We attempt to reproduce the entire foam quality scan, $f_g = 0.1$ to 1.0, by using a single velocity exponent (c=1/5.5). The degree of match is shown in Fig. 3, displaying pressure gradient profiles as function of gas rate (3a), and function of water rate (3b), and a contour plot showing effective viscosity μ_f as a function of both water and gas rates (Fig. 4). At a constant total flow rate, μ_f increases with decreasing gas fraction in the high-quality regime, shifting to decreasing μ_f with further decreasing gas fraction in the low-quality regime. As most of the data points correlates with the contour color, we have obtained a good match throughout the different rates and foam qualities.

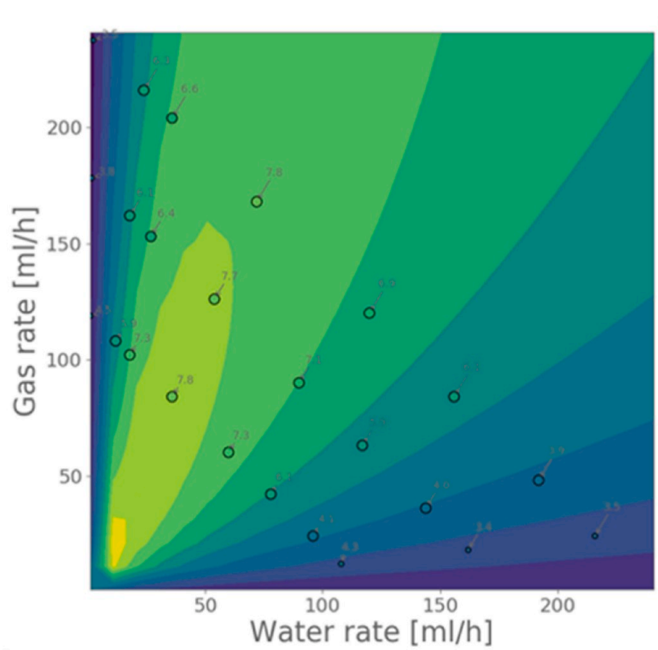

Fig. 4. Contour plot of effective NP foam viscosity, μ_f, [mPas] as a function of water and gas injection rates. Effective viscosity increases with decreasing gas fraction in the high-quality regime and decreases with further decreasing gas fraction in the low-quality regime. Degree of match is indicated by the color map.

2.2. NP CO_2 foam characterization by population-balance modeling

Previously, two distinct regimes have been identified for foam flow (Osterloh and Jante, 1992; Vassenden and Holt, 1998), a low-quality (wet foam) regime and a high-quality (dry foam) regime separated by a transition zone. Foam viscosity has been reported to be a function of these flow regimes (Alvarez et al., 2001) partially explaining the inconsistent rheological behavior reported in the literature. We find a moderate shear-thickening behavior at high NP foam quality (f_g=0.9) and a shear-thinning behavior at low NP foam quality (f_g=0.5) when plotting effective gas viscosity against total injection rate (Fig. 5), corroborating previous observations of SF foam (Alvarez et al., 2001). The transition from shear-thinning to shear-thickening NP foam flow emerges around gas fraction $f_g = 0.85$ (Fig. 2). Further, we observe that the effective viscosity μ_f of NP foam stabilizes as the total flow rate increases (near-well conditions). It appears that the experimental data that we are matching, are from a less-sensitive range of the spectrum as illustrated in Fig. 5, where the experimental f_g data (points) and simulation data f_g (lines) are displayed in corresponding colors. More experimental data are needed for a wider range of flow rates to completely map the influence of foam quality and flow rate on NP CO_2 flow properties. Our preliminary results indicate that the viscosity of NP CO_2 foam depends on foam quality below a certain threshold rate (≈200 ml/h for f_g = 0.9). Above this threshold, flowing NP foam appears near-Newtonian and less sensitive to injection rates and gas fractions. There have been reported near-Newtonian properties for SF foam (Ettinger and Radke, 1992; Persoff et al., 1991) due to increased snap-off frequency at higher liquid velocities. This effect is partially included in the simulation model, where the foam generation is dependent on gas and liquid velocities.

The effective viscosity μ_f during NP foam flow was about an order of magnitude higher than water, and the residual saturation values during steady state NP CO_2 foam approached the connate water saturation for a range of gas fractions. At high f_g (0.9), the baseline co-injection resulted in final water saturation of $S_w = 0.55$, compared with $S_w = 0.30$ for NP foam. Dynamic water profiles during the baseline fluid displacements (Fig. 6) were horizontal at all time steps during the co-injection. Hence, there was not a well-defined displacement front and the poor mobility ratio between CO_2 and water resulted in viscous fingering, leaving behind unswept zones of high water content in the pore system. In contrast, a distinct fluid displacement front developed during NP foam progression, and the front sharpened over time to become more piston-like.

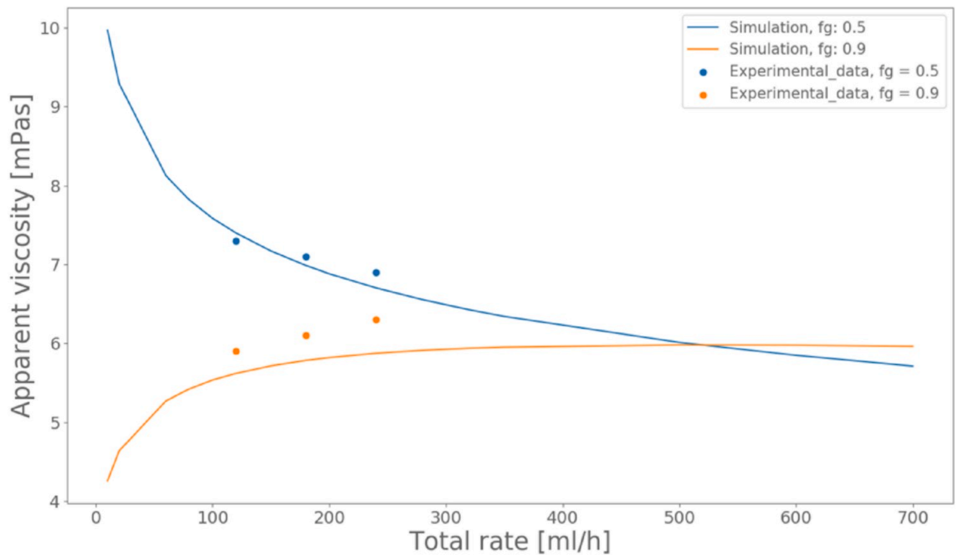

Fig. 5. Effective viscosity, μ_f, versus injection rate for $c = 1/5.5$ at two different gas fractions, $f_g = 0.5$ (blue) and $f_g = 0.9$ (orange), indicating shear-thinning trend at low NP foam quality and shear-thickening trend at high NP foam quality. The sensitivity decreases with increasing total flow rate.

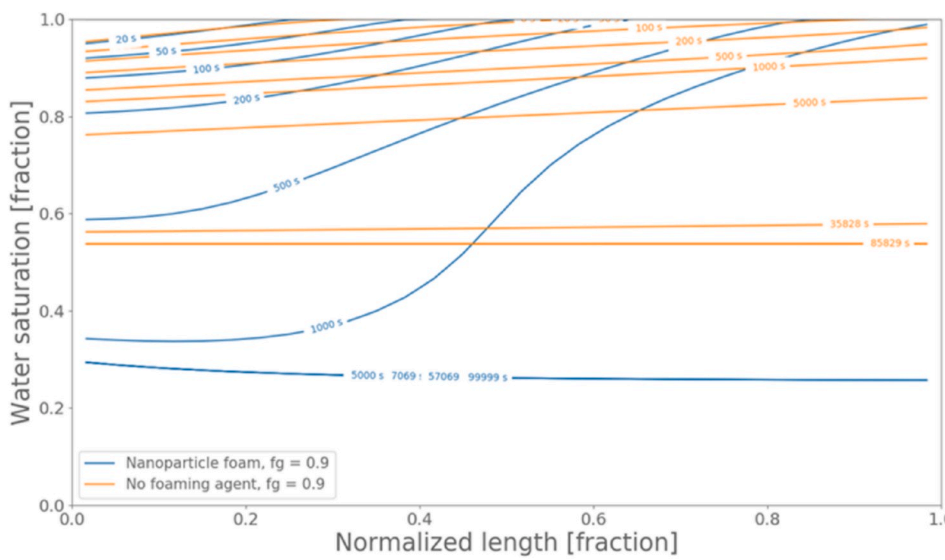

Fig. 6. Simulated water saturation as a function of normalized core length at constant $f_g = 0.9$, for NP foam (blue line) and for baseline (orange) without foaming agent. NP foam developed a distinct displacement front eventually (at 1000 s = 0.43 PV – pore volume), and improved the volumetric sweep compared to co-injection of CO_2 and water (no foaming agent).

Based on the dynamic water profiles in Fig. 6, it is clear that the NP foam generation is not instantaneous. A certain time is needed to generate strong foam to efficiently displacing the initial water. The development of bubbles (n_f) along the core length during NP foam flow provided additional important information on the foam generation process (Fig. 7). A shift in n_f occurred between 200 s and 500 s, indicating increased foam generation kinetics and finer foam texture. This change in kinetics was directly linked to the development of a distinct displacement front in Fig. 6 occurring at the same time step. During the transient flow period, some n_f profiles exceeded the steady-state texture, likely due to gas compressibility effects (Kovscek et al., 1995). Coalescence forces coarsened the foam texture over time and n_f profiles at steady-state conditions (5000 s = 2.2 PV and 99999 s = 43 PV) retained similar shapes as time step 500 s. After foam breakthrough at the outlet (normalized length = 1.0), a non-zero n_f value is present at the inlet (normalized length = 0.0), possibly due to a backward front movement of finer foam texture (Simjoo and Zitha, 2020; Apaydin and Kovscek, 2001; Almajid et al., 2019). At steady state, bubbles appeared across the entire core length, with a close-to-linear increase toward the outlet end. In proximity to the outlet of the core sample, the n_f value approached the theoretical foam density limit n^* at steady-state conditions.

Steady state NP and SF effective viscosity profiles highlighted that at current conditions SF CO_2 foam shifted maximum μ_f toward higher foam quality (f_g=0.9) and significantly enhanced the effective gas viscosity (see Fig S2 in Supplementary material). A previous study successfully modelled combined NP and SF foam flow at near-well conditions using a SF foam mechanistic framework, with lamella division as the dominant foam generation mechanism (Prigiobbe et al., 2016). They reported a synergetic effect of enhanced gas mobility reduction from combining the two foaming agents. We assume the main differences between the two systems (NP CO_2 foam versus SF CO_2 foam) in our paper are the average foam texture (Fig. 8) and the limiting capillary pressure, P_c^*. The average foam texture, n_f, obtained at steady state is consistently lower (factor

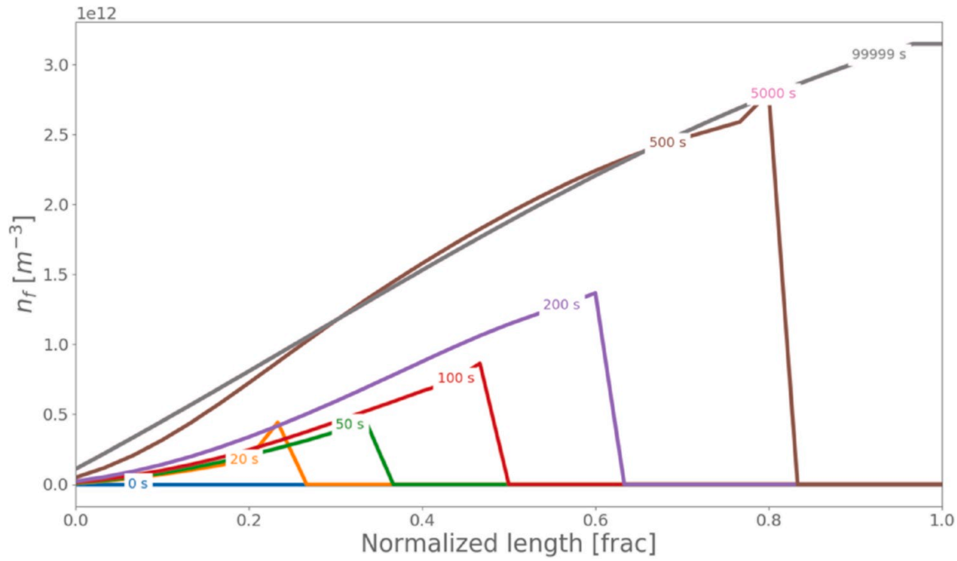

Fig. 7. Foam texture (n_f) development as function of normalized core length for NP foam at constant $f_g = 0.9$. The first time steps (20, 50, 100 and 200s) follow a similar foam profile with a gradual increase in number of lamellae ($\times$ 10^{12} m^{-3}). During the transient flow period, the density profiles temporarily exceeded the steady-state texture (500 s < t < 3000 s; not shown in Fig. 7), due to gas compressibility effects.

2.1) in the low-quality regime for NP foam. Further, the foam texture profile for NP foam collapses earlier than for SF foam due to a lower P_c^* value represented here. Because P_c^* strongly depends on foaming agent concentrations (Apaydin and Kovscek, 2001; Aronson et al., 1994), this effect was considerable for the current experimental data. Instead of a direct performance comparison between NP and SF foam, this study emphasizes dynamic foam textures to accurately describe NP CO_2 foam behavior and mobility control potential at low particle concentration (0.15 wt%). Modeling NP foam instead of SF foam impacted the kinetic expressions k_1 (foam creation) and k_{-1} (foam destruction), as well as the proportionality constant α and the velocity exponent c (detailed in Table 3).

3. Conclusions

Dynamic properties of CO_2 foam stabilized with nanoparticles (NP) were predicted using an established surfactant (SF) population-balance model, and led to the following key observations:

- The population-balance model matched experimental data of NP foam effective viscosity over a range of gas fractions, by reducing the shear-thinning effect commonly used for SF foam. This was supported by observations of near-Newtonian NP foam behavior in the laboratory at specific conditions. Foam viscosity appeared sensitive to quality regimes at low total flow rates (shear thinning for gas fraction $f_g = 0.5$, and shear thickening for $f_g = 0.9$).
- Simulations revealed that high-quality NP foam developed a distinct displacement front and improved local and overall sweep compared to co-injection of CO_2 and water (baseline; contained no foaming agents). Characteristics of the flowing foam were increased effective viscosity and decreased residual water saturation along the core length.

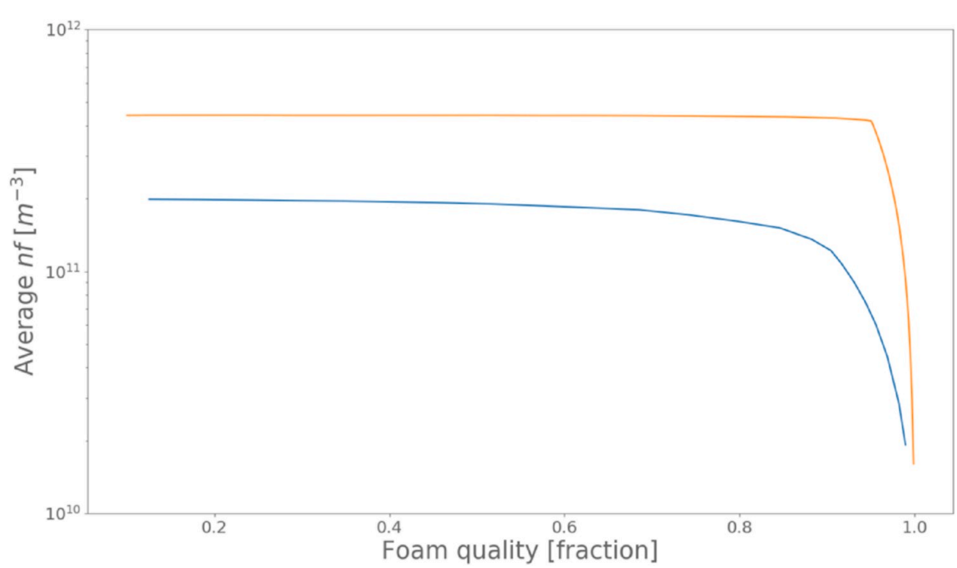

Fig. 8. Average foam texture, n_f [m^{-3}], simulated at steady-state conditions as a function of gas fractions for NP foam (blue) and SF foam (orange). The foam texture is consistently higher by a factor of 2.1 in favor of SF foam. Further, SF foam behavedmore stable than NP foam in the high-quality regime. In both cases, the average foam texture appeared constant over a wide range of gas fractions.

- At steady-state conditions, NP foam bubbles appeared across the entire core length, and the profiles showed increasing density of lamellae with distance within the sample. This led to reduced CO_2 mobility and improved displacement efficiency of low-concentration NP foam compared to baseline co-injections. Compared to high-concentration SF foam, the NP foam texture appeared coarser with lower effective viscosity, mainly ascribed to reduced bubble density and reduced limiting capillary pressure.

Declaration of competing interest

The authors declare that they have no known competing financial interests or personal relationships that could have appeared to influence the work reported in this paper.

Acknowledgements

The authors gratefully acknowledge financial support from Nouryon and from the Research Council of Norway [grant numbers 249742 and 268216]. Additional data can be found in Supplementary material and by contacting Martin Fernø (Martin.Ferno@uib.no).

Appendix A. Supplementary data

Supplementary data to this article can be found online at https://doi.org/10.1016/j.jngse.2020.103378.

References

Almajid, M.M., Nazari, N., Kovscek, A.R., 2019. Modeling steady-state foam flow: hysteresis and backward front movement. Energy Fuels 33 (11), 11353–11363.
Alvarez, J.M., Rivas, H.J., Rossen, W.R., 2001. Unified model for steady-state foam behavior at high and low foam qualities. SPE J. 6 (3), 325–333.
AlYousif, Z., Almobarky, M., Schechter, D., 2018. Nanoparticles-stabilized CO2/brine emulsions at reservoir conditions: a new way of mitigating gravity override in CO2 floods. In: SPE Kingdom of Saudi Arabia Annual Technical Symposium and Exhibition. Society of Petroleum Engineers: Dammam, Saudi Arabia, p. 12.
Apaydin, O.G., Kovscek, A.R., 2001. Surfactant concentration and end effects on foam flow in porous media. Transport Porous Media 43 (3), 511–536.
Aronson, A.S., Bergeron, V., Fagan, M.E., Radke, C.J., 1994. The influence of disjoining pressure on foam stability and flow in porous media. Colloid. Surface. Physicochem. Eng. Aspect. 83 (2), 109–120.
Barifcani, A., Al-Yaseri, A.Z., Iglauer, S., Johns, M.L., Lebedev, M., Vogt, S.J., 2015. Pore-scale analysis of formation damage in Bentheimer sandstone with in-situ NMR and micro-computed tomography experiments. J. Petrol. Sci. Eng. 129, 48–57.
Belyadi, H., Fathi, E., Belyadi, F., 2017. Chapter five - hydraulic fracturing fluid systems. In: Belyadi, H., Fathi, E., Belyadi, F. (Eds.), Hydraulic Fracturing in Unconventional Reservoirs. Gulf Professional Publishing, Boston, pp. 49–72.
Benali, B., 2019. Quantitative Pore-Scale Analysis of CO2 Foam for CCUS. University of Bergen.
Bennetzen, M.V., Mogensen, K., 2014. Novel applications of nanoparticles for future enhanced oil recovery. In: International Petroleum Technology Conference, p. 14. International Petroleum Technology Conference: Kuala Lumpur, Malaysia.
Bernard, G.C., Holm, L.W., Harvey, C.P., 1980. Use of surfactant to reduce CO2 mobility in oil displacement. Soc. Petrol. Eng. J. 20 (4), 281–292.
Bertin, H.J., Quintard, M.Y., Castanier, L.M., 1998. Modeling transient foam flow in porous media using a bubble population correlation. In: SPE Annual Technical Conference and Exhibition. Society of Petroleum Engineers, New Orleans, Louisiana, p. 9.
Binks, B.P., 2002. Particles as surfactants—similarities and differences. Curr. Opin. Colloid Interface Sci. 7 (1), 21–41.
Binks, B.P., Lumsdon, S.O., 2000. Influence of particle wettability on the type and stability of surfactant-free emulsions. Langmuir 16 (23), 8622–8631.
Chang, S.H., Owusu, L.A., French, S.B., Kovarik, F.S., 1990. The effect of microscopic heterogeneity on CO2 -foam mobility: Part 2-mechanistic foam simulation. In: SPE/DOE Enhanced Oil Recovery Symposium. Society of Petroleum Engineers, Tulsa, Oklahoma, p. 14.
Chen, Q., Gerritsen, M.G., Kovscek, A.R., 2010. Modeling foam displacement with the local-equilibrium approximation : theory and experimental verification. SPE J. 15, 171–183.
Dickson, J.L., Binks, B.P., Johnston, K.P., 2004. Stabilization of carbon dioxide-in-water emulsions with silica nanoparticles. Langmuir 20 (19), 7976–7983.
Espinoza, D.A., Caldelas, F.M., Johnston, K.P., Bryant, S.L., Huh, C., 2010. Nanoparticle-stabilized supercritical CO2 foams for potential mobility control applications. In: SPE Improved Oil Recovery Symposium. Society of Petroleum Engineers, Tulsa, Oklahoma, USA, p. 13.
Ettinger, R.A., Radke, C.J., 1992. Influence of texture on steady foam flow in berea sandstone. SPE Reservoir Eng. 7 (1), 83–90.
Falls, A.H., Hirasaki, G.J., Patzek, T.W., Gauglitz, D.A., Miller, D.D., Ratulowski, T., 1988. Development of a mechanistic foam simulator: the population balance and generation by snap-off. SPE Reservoir Eng. 3 (3), 884–892.
Falls, A.H., Musters, J.J., Ratulowski, J., 2007. The apparent viscosity of foams in homogeneous bead packs. SPE Reservoir Eng. 4 (2), 155–164.
Fernø, M.A., Gauteplass, J., Pancharoen, M., Haugen, Å., Graue, A., Kovscek, A.R., Hirasaki, G., 2016. Experimental study of foam generation, sweep efficiency, and flow in a fracture network. SPE J. 21 (4), 1140–1150.
Griffith, N., Ahmad, Y., Daigle, H., Huh, C., 2016. Nanoparticle-stabilized natural gas liquid-in-water emulsions for residual oil recovery. In: SPE Improved Oil Recovery Conference. Society of Petroleum Engineers, Tulsa, Oklahoma, USA, p. 22.
Heller, J.P., Kuntamukkula, M.S., 1987. Critical review of the foam rheology literature. Ind. Eng. Chem. Res. 26 (2), 318–325.
Hematpur, H., Mahmood, S.M., Nasr, N.H., Elraies, K.A., 2018. Foam flow in porous media: concepts, models and challenges. J. Nat. Gas Sci. Eng. 53, 163–180.
Hirasaki, G.J., Lawson, J.B., 1985. Mechanisms of foam flow in porous media: apparent viscosity in smooth capillaries. Soc. Petrol. Eng. J. 25 (2), 176–190.
Horjen, H., 2015. CO2 Foam Stabilization with Nanoparticles and EOR in Fractured Carbonate Systems. University of Bergen.
Kam, S.I., Rossen, W.R., 2003. A model for foam generation in homogeneous media. SPE J. 8 (4), 417–425.
Karambeigi, M.S., Abbassi, R., Roayaei, E., Emadi, M.A., 2015. Emulsion flooding for enhanced oil recovery: interactive optimization of phase behavior, microvisual and core-flood experiments. J. Ind. Eng. Chem. 29, 382–391.
Khatib, Z.I., Hirasaki, G.J., Falls, A.H., 1988. Effects of capillary pressure on coalescence and phase mobilities in foams flowing through porous media. SPE Reservoir Eng. 3 (3), 919–926.
Kim, I., Taghavy, A., DiCarlo, D., Huh, C., 2015. Aggregation of silica nanoparticles and its impact on particle mobility under high-salinity conditions. J. Petrol. Sci. Eng. 133, 376–383.
Kim, I., Worthen, A.J., Johnston, K.P., DiCarlo, D.A., Huh, C., 2016. Size-dependent properties of silica nanoparticles for Pickering stabilization of emulsions and foams. J. Nanoparticle Res. 18 (4), 1–12.
Kolb, W.B., Cerro, R.L., 2002. The motion of long bubbles in tubes of square cross section*. Phys. Fluid. Fluid Dynam. 5 (7), 1549–1557.
Kovscek, A.R., Radke, C.J., 1994. Fundamentals of foam transport in porous media. In: Foams: Fundamentals and Applications in the Petroleum Industry. American Chemical Society, pp. 115–163.
Kovscek, A.R., Patzek, T.W., Radke, C.J., 1995. A mechanistic population balance model for transient and steady-state foam flow in Boise sandstone. Chem. Eng. Sci. 50 (23), 3783–3799.
Leverett, M., 1941. Capillary behavior in porous solids. Trans. AIME 142 (1), 152–169.
Liaw, H.K., Kulkarni, R., Chen, S., Watson, A.T., 1996. Characterization of fluid distributions in porous media by NMR techniques. AIChE J. 42 (2), 538–546.
Lotfollahi, M., Kim, I., Beygi, M.R., Worthen, A.J., Huh, C., Johnston, K.P., Wheeler, M. F., DiCarlo, D.A., 2016a. Experimental studies and modeling of foam hysteresis in porous media. In: SPE Improved Oil Recovery Conference. Society of Petroleum Engineers, Tulsa, Oklahoma, USA, p. 18.
Lotfollahi, M., Farajzadeh, R., Delshad, M., Varavei, A., Rossen, W.R., 2016b. Comparison of implicit-texture and population-balance foam models. J. Nat. Gas Sci. Eng. 31, 184–197.
Ma, K., Ren, G., Mateen, K., Morel, D., Cordelier, P., 2015. Modeling techniques for foam flow in porous media. SPE J. 20 (3), 453–470.
Marsden, S.S., Khan, S.A., 1966. The flow of foam through short porous media and apparent viscosity measurements. Soc. Petrol. Eng. J. 6 (1), 17–25.
Mo, D., Yu, J., Liu, N., Lee, R.L., 2012. Study of the Effect of Different Factors on Nanoparticle-Stablized CO2 Foam for Mobility Control. SPE Annual Technical Conference and Exhibition.
Nguyen, Q.P., Alexandrov, A.V., Zitha, P.L., Currie, P.K., 2000. Experimental and modeling studies on foam in porous media: a review. In: SPE International Symposium on Formation Damage Control. Society of Petroleum Engineers, Lafayette, Louisiana, p. 22.
Ortiz, D., Izadi, M., Kam, S.I., 2019. Modeling of nanoparticle-stabilized CO2 foam enhanced oil recovery. SPE Reservoir Eval. Eng. 22 (3), 971–989.
Osterloh, W.T., Jante Jr., M.J., 1992. Effects of gas and liquid velocity on steady-state foam flow at high temperature. In: SPE/DOE Enhanced Oil Recovery Symposium. Society of Petroleum Engineers, Tulsa, Oklahoma, p. 12.
Peksa, A.E., Wolf, K.H.A.A., Zitha, P.L.J., 2015. Bentheimer sandstone revisited for experimental purposes. Mar. Petrol. Geol. 67, 701–719.
Persoff, P., Radke, C.J., Pruess, K., Benson, S.M., Witherspoon, P.A., 1991. A laboratory investigation of foam flow in sandstone at elevated pressure. SPE Reservoir Eng. 6 (3), 365–372.
Prigiobbe, V., Worthen, A.J., Johnston, K.P., Huh, C., Bryant, S.L., 2016. Transport of nanoparticle-stabilized CO2-foam in porous media. Transport Porous Media 111 (1), 265–285.
Rognmo, A.U., 2018. CO2 Foams for Enhanced Oil Recovery and CO2 Storage. University of Bergen.
Rognmo, A.U., Horjen, H., Fernø, M.A., 2017. Nanotechnology for improved CO2utilization in CCS: laboratory study of CO2-foam flow and silica nanoparticle retention in porous media. Int. J. Greenh. Gas Contr. 64 (March), 113–118.
Rognmo, A.U., Al-Khayyat, N., Heldal, S., Vikingstad, I., Eide, Ø., Fredriksen, S.B., Alcorn, Z.P., Graue, A., Bryant, S.L., Kovscek, A.R., Fernø, M.A., 2019. Performance of silica nanoparticles in CO2 foam for EOR and CCUS at tough reservoir conditions. SPE J. 10.

Simjoo, M., Zitha, P.L.J., 2020. Modeling and experimental validation of rheological transition during foam flow in porous media. Transport Porous Media 131 (1), 315–332.

Sun, X., Zhang, Y., Chen, G., Gai, Z., 2017. Application of nanoparticles in enhanced oil recovery: a critical review of recent progress. Energies 10 (3).

Vassenden, F., Holt, T., 1998. Experimental foundation for relative permeability modeling of foam. In: SPE/DOE Improved Oil Recovery Symposium. Society of Petroleum Engineers, Tulsa, Oklahoma, p. 11.

Worthen, A., Taghavy, A., Aroonsri, A., Kim, I., Johnston, K., Huh, C., Bryant, S., DiCarlo, D., 2015. Multi-scale evaluation of nanoparticle-stabilized CO2-in-Water foams: from the benchtop to the field. In: SPE Annual Technical Conference and Exhibition. Society of Petroleum Engineers, Houston, Texas, USA, p. 13.

Xiao, C., Balasubramanian, S.N., Clapp, L.W., 2017. Rheology of viscous CO2 foams stabilized by nanoparticles under high pressure. Ind. Eng. Chem. Res. 56 (29), 8340–8348.

Yekeen, N., Manan, M.A., Idris, A.K., Padmanabhan, E., Junin, R., Samin, A.M., Gbadamosi, A.O., Oguamah, I., 2018. A comprehensive review of experimental studies of nanoparticles-stabilized foam for enhanced oil recovery. J. Petrol. Sci. Eng. 164 (August 2017), 43–74.

Yu, J., Khalil, M., Liu, N., Lee, R., 2014. Effect of particle hydrophobicity on CO2 foam generation and foam flow behavior in porous media. Fuel 126, 104–108.

Zhang, T., Davidson, D., Bryant, S.L., Huh, C., 2010. Nanoparticle-stabilized emulsions for applications in enhanced oil recovery. In: SPE Improved Oil Recovery Symposium. Society of Petroleum Engineers, Tulsa, Oklahoma, USA, p. 18.

Zhou, Y., Wang, D., Wang, Z., Cao, R., 2017. The formation and viscoelasticity of pore-throat scale emulsion in porous media. Petrol. Explor. Dev. 44 (1), 111–118.